Revision 2

Word count: 7696

The use of boron nitride to impose reduced redox conditions in experimental petrology

Huijuan Li[1], Hugh St.C. O'Neill[2], Lifei Zhang[1]*, Xinjian Bao[1], Xi Liu[1]

[1]MOE Key Laboratory of Orogenic Belts and Crustal Evolution, School of Earth and Space Sciences, Peking University, No. 5 Yiheyuan Road, Haidian District, Beijing, 100871, China

[2]School of Earth, Atmosphere and Environment, Monash University, Clayton, VIC 3800, Australia.

*Corresponding author.

Email address: lfzhang@pku.edu.cn (L. Zhang).

Abstract

BN is a commonly used pressure transmitting material in experimental petrology. It is often considered to be as inert as MgO or Al_2O_3, and its redox potential is seldomly discussed. It is generally implied that, when used as a capsule sleeve, BN may impose relatively reduced conditions, similar to the effect of the fayalite-magnetite-quartz (FMQ) buffer. However, sediment melting experiments performed at 1050°C and 3 GPa with BN as the capsule sleeve, produced a hydrous rhyolitic melt with dissolved H_2S and CH_4 (Li et al. 2021). The resulting fO_2 estimate is significantly more reduced than that for the magnetite-wustite (MW)-buffered experiment where H_2S and CH_4 were undetected (Li et al. 2021), possibly to the extent of the quartz-iron-fayalite (QIF) buffered conditions produced when BN is used as a capsule or crucible (Wendlandt et al. 1982). In order to establish an explanation for such a discrepancy, we have

conducted further investigation to better constrain the fO_2 imposed by BN, when used as a capsule sleeve. Here we report results on analyses of Fe content in Au capsules, a comparative experiment using a QIF buffer and an experiment with an Fe-(Mg,Fe)O sensor for direct analysis of fO_2. The calibration of the equilibrium between FeO in melt and Fe in the Au capsule, from Ratajeski and Sisson (1999) appears to be inadequate in constraining fO_2 for our experiments. However, we were able to obtain Fe diffusion coefficients in Au from the Fe diffusion profiles observed in the capsule of the Fe-(Mg,Fe)O sensor experiment, and both the inner and outer capsules of the MW-buffered experiment, with resulting values of 1×10^{-13} m^2/s, 3×10^{-14} m^2/s, and 5×10^{-14} m^2/s, respectively. The QIF-buffered and Fe-(Mg,Fe)O sensor experiments provide several lines of evidence supporting the observation that BN imposes QIF-like redox conditions. Firstly, the Fe-(Mg,Fe)O sensor returned an fO_2 value of QIF. Secondly, the "apparent" partition coefficients between FeO content in melt and Fe in the Au capsules are similar between the BN experiment and the QIF-buffered experiment. Thirdly, we observe CH_4 and H_2O peaks with similar intensities in the Raman spectra of melts from these two experiments, suggesting similar H_2 and thus O_2 fugacity. As our experiments were performed on a cubic press with the experimental assembly encased in a pyrophyllite cube, we interpret that the significantly reduced conditions imposed by BN are likely due to high H_2O activity maintained by dehydration of pyrophyllite, which can be explained using the reaction $2BN+3H_2O=B_2O_3+N_2+3H_2$. Lower H_2O activity will reduce or inhibit the oxidation of BN and its fO_2 buffering ability. If heat-treated, BN acts as a highly efficient H_2 barrier, as shown by Truckenbrodt et al. (1997). Through our efforts to determine the fO_2 imposed by using BN as a capsule sleeve in our experimental assembly, we are able to demonstrate the reducing ability of BN as an assembly component, and furthermore shed light on the process by which BN imposes such reduced fO_2. We hereby

present what we have learnt during the course of this investigation, in the hope that the effect of BN on fO_2 control is both recognized and further exploited in future experimental studies.

Keywords:

BN, oxygen fugacity control, Fe in Au calibration, Fe-(Mg,Fe)O sensor, experimental petrology

Introduction

Boron Nitride (BN) is an often-used pressure transmitting material in experimental petrology; however, it has been considered to be as inert as MgO or Al_2O_3, and its redox potential has seldomly been discussed. The use of BN as a capsule material or crucible for silicate systems has been previously reported (Mysen 1979; Mysen and Popp 1980), but did not gain wide popularity due to the fact that BN imposes highly reducing conditions; and furthermore that B_2O_3, produced through oxidation of BN, acts as a fluxing agent for melting (Wendlandt et al. 1982). Based on the BN oxidation reaction

$$2BN+3/2O_2=B_2O_3+N_2 \quad (1),$$

Wendlandt et al. (1982) estimated that the fO_2 imposed by BN capsules is ~3 log units below the quartz-iron-fayalite (QIF) buffer at 1027°C and 1 bar for pure N_2 conditions; while for 1027°C and 3 GPa conditions, the estimated fO_2 is close to that of the QIF buffer. Note that such a difference arises from the different N_2 fugacity between 1 bar and 3 GPa. The reducing ability of BN was verified by Wendlandt et al. (1982) with experiments performed using BN capsules containing various starting materials. They showed that FeO and NiO were reduced to Fe and Ni

metal respectively; Fe metal was also produced in experiments with either olivines of various compositions or a garnet lherzolite as starting materials.

The redox imposing character of BN initially came to our attention after a sediment melting experiment performed in a previous study (Li et al. 2021; exp. LMD670) at 3 GPa, 1050°C using BN as a capsule sleeve and spacer, produced a hydrous rhyolitic melt with dissolved H_2S and CH_4, as shown by the Raman spectra of the quenched melt (Fig. 1). Dissolution of CH_4 in silicate melt has been reported mainly in experiments performed at reduced conditions where a metal alloy phase is stable (i.e., fO_2<IW, IW stands for iron-wustite buffer) (Kadik et al. 2006, 2015, 2017; Mysen et al. 2009; Ardia et al. 2013; Dasgupta et al. 2013; Armstrong et al. 2015; Li et al. 2015, 2016; Dalou et al. 2019; Grewal et al. 2020). Moreover, H_2S and CH_4 were undetected in the melt from the magnetite-wustite (MW)-buffered experiment in the same series with identical starting composition and *PT* conditions (Fig. 1). We therefore interpret that the intrinsic fO_2 imposed by the BN capsule sleeve and spacer is lower than that of the MW buffer. In addition, graphite was a stable phase in the MW-buffered experiment, but absent in the BN experiment, also suggesting that BN imposes more reduced conditions than the MW buffer. The absence of graphite in the BN experiment (LMD670) provides an upper-bound constraint on the fO_2 of the experiment. The fO_2 limit for graphite stability can be calculated based on the reaction $C+2H_2O=CH_4+O_2$, with the equilibrium constant calculated according to Ohmoto and Kerrick (1977). Considering that the gas phase in equilibrium with the experimental charge should be dominated by CH_4, we can assume fCH_4 as being equal to that of pure CH_4 at *PT* conditions of 3 GPa, 1050°C (calculated using the CHO program). In combination with the H_2O fugacity estimated based on H_2O content in melt (Li et al. 2021), the calculated fO_2 is ~FMQ-5.5. During the course of our previous study (Li et al. 2021), no independent assessment was attempted to

directly determine the fO_2 for the BN experiment. We thus assumed that the fO_2 imposed by BN would be similar to that of the QIF buffer, as calculated for the BN capsule at 3 GPa, 1050°C. This appeared to be a reasonable assumption considering that the data point for the BN experiment fits the trend of variation of melt S solubility with fO_2, and also agrees with the model prediction of Clemente et al. (2004). On a separate note, the presence of pyrrhotite, rather than Fe metal in exp. LMD670 at such reduced conditions can be attributed to its high $\log fS_2$, estimated to be -2.2 (Li et al. 2021), higher than the calculated $\log fS_2$ (-2.6 at 3 GPa, 1050°C) for Fe metal and FeS coexistence based on the reaction $Fe+1/2S_2=FeS$.

A search of the literature revealed that the reducing effect of BN when used as pressure transmitting material has been indirectly observed before. For example, Fe loss to Au capsules was reported by Ratajeski and Sisson (1999). Their experiments investigated melting of natural hornblende quartz gabbro at 8 kbar, 800-975°C with an estimated bulk H_2O content of ~1.3 wt%. In their NaCl-graphite experimental assembly, BN powder was packed around the Au capsule to minimize oxidation of the sample. Based on the analyses of Fe content in Au capsules and FeO content in melt, they obtained an expression for the apparent equilibrium constant (K') of the reaction

$$FeO(melt)=Fe(Au\ capsule)+0.5O_2 \quad (2)$$

$$\ln K'=-22.953[1000/T(K)]+3.421 \quad (r^2=0.99) \quad (3)$$

with K' defined as

$$K' = \frac{X_{Fe}^{alloy} \times {fO_2}^{0.5}}{X_{FeO}^{melt}} \quad (4)$$

which is in effect representing the distribution coefficient since the activity coefficients for Fe in Au (γ_{Fe}^{alloy}) and FeO in melt (γ_{FeO}^{melt}) were not calculated. The fO_2 value used in the calibration was assumed to be FMQ-1, which was based on the fO_2 estimation for similar experiments from

This is the peer-reviewed, final accepted version for American Mineralogist, published by the Mineralogical Society of America.
The published version is subject to change. Cite as Authors (Year) Title. American Mineralogist, in press.
DOI: https://doi.org/10.2138/am-2022-8577. http://www.minsocam.org/

Patiño Douce and Beard (1994, 1995), although the latter experiments were performed without BN in their experimental assembly. When Fe content in Au capsules and FeO content in melt are known, fO_2 can in turn be derived from calculated K' values:

$$\log fO_2 = 2 \times \frac{\ln K' - \ln X_{Fe}^{alloy} + \ln X_{FeO}^{melt}}{\ln(10)} \quad (5)$$

Sisson et al. (2005) performed hydrous (1.7-2.3 wt% H_2O) basalt melting experiments at 700 MPa with either BN or NaCl as capsule sleeves, and reported that sulfide was stable in experiments using BN, while titanomagnetite was stable in experiments using NaCl. The fO_2 for the former case was estimated to be similar to FMQ-buffered experiments, while the fO_2 for the latter was estimated to be between FMQ and (Re-ReO_2)-buffered conditions. Most recently, Pelleter et al. (2021) reported S contents at sulfide saturation (SCSS) in hydrous rhyolitic melts, produced by melting of Ca-poor pelite at 3 GPa, 750-1000°C using a Talc-pyrex-graphite assembly, but with either MgO or BN capsule sleeves. Higher SCSS values were obtained for experiments using MgO than those using BN as capsule sleeves. For example, the SCSS value was reported to be ~150 ppm for the experiment performed at 800°C with a bulk S content of 2.1 wt% when using a BN capsule sleeve, but reached ~830 ppm for the 750° C experiment where a MgO capsule sleeve was used. Such a difference in melt S content reflects the higher fO_2 conditions imposed by MgO with respect to BN. In summary, it is clear that the use of BN in these experimental studies imposed reduced conditions (≤FMQ). However, the estimated fO_2 conditions were not as reduced as those we have empirically observed in our own study (<MW, likely equivalent to QIF).

To better constrain the intrinsic fO_2 of our experimental assembly using BN as a capsule sleeve, new experiments have been conducted and assessed in combination with further analyses of experiments from our previous work. Inspired by the work of Ratajeski and Sisson (1999), we

have analyzed the post-run Fe content in Au capsules from the experimental series. We also report an additional experiment with identical starting composition and *PT* conditions to those previously reported, but with a QIF buffer, which serves as a comparison to the BN experiment. An experiment employing an Fe-(Mg,Fe)O sensor as the starting material and BN as the capsule sleeve, has been performed for direct analysis of the experimental fO_2. The application of BN in fO_2 control will also be discussed.

Methods

Experimental methods

A detailed description of both the experimental design and the method for fO_2 estimation are presented in Li et al. (2021). Here we briefly describe the key points. All of the experiments, both new and previously reported, have been conducted using a CS-IV 6 ×14 MN cubic press at the High Pressure and High Temperature laboratory, Peking University. The experimental assembly (BJC-11) has a cylindrical configuration, which is comprised of a BN outer sleeve, graphite heater, and a BN/MgO spacer and capsule sleeve, similar to the common assembly used in piston-cylinder experiments, the primary difference being that the cylindrical unit is further encased in a pyrophyllite cube with an edge length of 32.5 mm (Fig. 2). For experiments with buffer assemblies, a double-capsule configuration is employed with an inner capsule (2.5 mm O.D.) containing ~10 mg starting material and an outer capsule (5 mm O.D.) containing 50-60 mg of buffer material together with 4-5 mg of deionized H_2O. Both inner and outer capsules are fabricated from Au tubing. Au is the preferred inert medium when the starting composition contains Fe and S, when compared to other potential capsule materials, e.g., Pb, Pd, etc. As the experimental series regarding sediment melting was intended to study sulfur solubility in

sediment melt as a function of oxygen fugacity, the starting composition used (EPSM-S1) has a major element composition similar to that of the average "global subducting sediment" (GLOSS) (Plank and Langmuir 1998), but with a sulfur content of ~1.9 wt%. Due to the low H_2O activity (~0.01) in the inner capsule estimated based on H_2O content in melt, the fO_2 in the inner capsule is generally ~2 log units lower than that imposed by the buffer.

Both the QIF-buffered exp. LMD776 and the Fe-(Mg,Fe)O sensor exp. LMD783 were performed at 3 GPa, 1050°C; identical to the *PT* conditions of the previous experimental series (Table 1). The QIF buffer assemblage has a mixing ratio of 1:1:1 between SiO_2, Fe metal powder and fayalite. For the Fe-(Mg,Fe)O sensor experiment, the starting composition was a mix of Fe metal powder and $Mg(OH)_2$ in order to achieve H_2O-saturated conditions. The resultant Fe:MgO mixing ratio was 3:1.

Analytical methods

The measurement of Fe in Au capsules was accomplished using an electron microprobe (JEOL JXA 8230) at Peking University. By employing beam conditions of 20 kV and 50 nA and a counting time of 60 s, a detection limit of ~55 ppm can be achieved. The diffusion profiles of Fe in Au capsules have also been obtained across both the inner and outer capsule walls, with a step size of 20 μm.

The analysis of S content in melt was performed on the same electron microprobe, employing a PETH analyzing crystal, in combination with a defocused beam of 15 kV and 50 nA, and 100 s counting time. The resultant detection limit was ~20 ppm. ZnS was used as the calibration standard.

This is the peer-reviewed, final accepted version for American Mineralogist, published by the Mineralogical Society of America.
The published version is subject to change. Cite as Authors (Year) Title. American Mineralogist, in press.
DOI: https://doi.org/10.2138/am-2022-8577. http://www.minsocam.org/

The Raman spectra of melts were recorded with a Horiba LabRam HR Evolution spectrometer at Peking University, employing a Nd:YAG laser with a wavelength of 532 nm and an emission power of 80 mW. The recording conditions are as follows: 100× objective lens, 100% laser power, 600 grating and 500 μm pinhole. Acquisition time was 10s for each window, accumulated over 3 scans.

Results

Fe content in Au capsules

For exp. LMD670, the profile of Fe in the Au capsule appears as a flat line, indicating an equilibrium between the sample and the capsule (Fig. 3a). The average Fe content in the Au capsule is about 0.072±0.004 wt%; while the FeO content in melt is 0.32±0.05 wt%. Therefore an "apparent" Fe partition coefficient between melt and the Au capsule, calculated as the ratio between FeO in melt and Fe in Au, is ~4.4. According to the calibration of Ratajeski and Sisson (1999) (Eq. 3 and 5), the fO_2 for exp. LMD670 is calculated to be ~FMQ-3.5, which is ~2 log units higher than the upper limit estimated based on graphite stability.

For the MW-buffered exp. LMD690, the profile of Fe in the Au inner capsule shows a general increasing trend from the sample-inner capsule boundary to the inner capsule-buffer boundary (Fig. 3b), which can be attributed to the diffusion of Fe from the buffer inwards. However, on closer inspection, the profile begins with a section (~40 μm) of decreasing Fe content, which may represent the diffusion of Fe from the sample to the Au capsule. Analyses of Fe in Au close to the sample returned an average of 0.083±0.007 wt%. With an FeO content of 0.86±0.07 wt% in melt, the "apparent" Fe partition coefficient between melt and the Au capsule is ~10.4, suggesting the fO_2 is ~0.8 log units higher than that for exp. LMD670. Such a variance in fO_2 is

far smaller than what would have been anticipated. This may be due to the fact that Fe partitioning between the sample and the Au capsule had yet to reach equilibrium. If we take the lowest point of the profile (Fig. 3b), 0.021 wt%, which is the apparent meeting point of the two diffusion sections, the calculated difference in fO_2 is ~2 log units.

The QIF-buffered experiment

For the QIF-buffered exp. LMD776, the profile of Fe in the inner Au capsule also shows a general increasing trend from the sample towards the buffer (Fig. 3d), reflecting the diffusion of Fe from the buffer inwards. The wavy pattern observed in the Fe concentration profiles for both inner and outer Au capsules may indicate a progressive approach toward equilibrium (Fig. 3d, e). The capsule Fe content is generally higher than that observed for the MW-buffered exp. LMD690, which may arise from either the lower fO_2 or the faster diffusion rate of metallic Fe due to a higher concentration gradient or a combination of both. The Fe content in the region of the Au capsule close to the sample has an average of 0.30±0.04 wt%, while the FeO content in melt is 1.36±0.04 wt%, resulting in an apparent partition coefficient of ~4.5, similar to that for exp. LMD670. The fact that the beginning of the profile shows a minimal slope (Fig. 3d) may suggest equilibrium has been attained between the sample and the Au capsule. If this is indeed the case, the fO_2 imposed by the BN capsule sleeve would appear to be similar to that of the QIF buffer.

The post-run buffer assembly has a rather interesting morphology, which is worth documenting (Fig. S1). Note that we are observing only one longitudinal cross-section of the capsule, and as such the possibility of heterogeneous distribution of buffer materials latitudinally cannot be ruled out. Large olivine and ferrosilite crystals form a shell surrounding the inner

This is the peer-reviewed, final accepted version for American Mineralogist, published by the Mineralogical Society of America.
The published version is subject to change. Cite as Authors (Year) Title. American Mineralogist, in press.
DOI: https://doi.org/10.2138/am-2022-8577. http://www.minsocam.org/

capsule. The formation of ferrosilite may be due to the reaction of Fayalite and SiO_2, or alternatively to the reduction of olivine, which produces ferrosilite and metallic Fe. At one end of the capsule, we observe the intergrowth of skeletal olivine and coesite between the olivine-ferrosilite layer and the outer capsule. While the Ferrosilite-fayalite-Fe assemblage imposes slightly lower fO_2 than QIF (Woodland and O'Neill 1997), it can be considered similar within the accepted degree of experimental uncertainty. We found no presence of Fe metal in the outer capsule, which may imply complete loss of Fe to the Au capsule, and consequently lower Fe activity. Woodland and O'Neill (1997) observed lowered H_2O activity in the QIF assemblage at 1.7 GPa, 700-1000°C due to increased solubility of silicates in H_2O at high pressure and high temperature. If the skeletal olivine and coesite represent quench crystal formation, i.e., high solubility of coesite and olivine at 3 GPa, 1050°C, then H_2O activity will also be significantly lowered. The final fH_2 in the outer capsule depends on the counterbalance of these two effects. The leveling off of the Fe profile in the outer capsule of exp. LMD776 (Fig. 3e) suggests that the buffer assemblage may have reached, or be close to reaching, equilibrium with the fH_2 imposed by the assembly.

The FeO content in the melt of exp. LMD776 is far higher than would be predicted for such low fO_2 conditions, as shown by the decreasing trend of FeO content in melt with decreasing fO_2 for our experimental series (Li et al. 2021). As depicted by the FeS saturation reaction

$$FeS(\text{sulfide solid/melt})+1/2O_2=FeO(\text{silicate melt})+1/2S_2 \quad (6),$$

at sulfide saturation, lower fO_2 leads to lower fS_2, or lower FeO content in melt, or both. We have observed decreasing trends for both fS_2 and FeO content in melt for our experimental series with fixed bulk S content (Li et al. 2021). The higher FeO content in the melt of exp. LMD776 may result from Fe contaminating the starting composition due to Fe diffusion from the buffer. The

This is the peer-reviewed, final accepted version for American Mineralogist, published by the Mineralogical Society of America.
The published version is subject to change. Cite as Authors (Year) Title. American Mineralogist, in press.
DOI: https://doi.org/10.2138/am-2022-8577. http://www.minsocam.org/

melt S content falls within the trend observed in our previous study, that is, the lnS (ppm) in melt has a negative linear correlation with $\ln X_{FeO}$ in melt with a slope close to -1 (Fig. 4). Such a correlation for low FeO (<~5 wt%) melts is predicted by the thermodynamic framework for modeling sulfur content in melt at sulfide saturation (SCSS) as a function of the standard state Gibbs free energy of the FeS saturation reaction (Eq. 6), sulfide capacity (C_S^{2-}), the activity of FeO in melt (a_{FeO}^{melt}) and the activity of FeS in sulfide melt ($a_{FeS}^{sulfide}$) (O'Neill and Mavrogenes 2002; O'Neill 2021); and in the case of hydrous rhyolitic melt with the relation (Li and Zhang 2022):

$$\ln[HS]_{SCSS} = -\Delta G^{\circ}_{Fes\text{-}FeO}/RT + \ln C_{HS} - \ln a_{FeO}^{melt} + \ln a_{FeS}^{sulfide} \quad (7),$$

where C_{HS} represents the hydrosulfide capacity, defined for the dissolution of H_2S in hydrous melt. Interested readers may find further details in the above references. The main point being that such an observation (Fig. 4) provides indirect evidence that the sample and the near side of the inner capsule may be at or close to an equilibrium state.

Further evidence supporting similar fO_2 conditions for exps. LMD670 and 776 comes from the Raman spectra of their respective melts (Fig. 1). Firstly, their spectra show similar patterns in terms of silicate peaks. As shown in our previous study, such patterns are notably different between reduced (FMQ-3.8 and below) and oxidized (FMQ-2.2 and above) experiments (see Fig. 4 of Li et al. 2021). Secondly, they present H_2O and CH_4 peaks with similar intensity, suggesting similar H_2O and CH_4 fugacity, and consequently similar H_2 and O_2 fugacity.

The Fe-(Mg,Fe)O sensor experiment

Fe diffusion into the Au capsule is observed clearly as a grey band under stereomicroscope for the Fe-(Mg,Fe)O sensor exp. LMD783 (Fig. 5a), demonstrating reduced redox conditions. The

achievement of equilibrium in the sample is demonstrated by the even distribution of Fe metal and (Mg,Fe)O in the sample (Fig. 5b), and by homogeneous (Mg,Fe)O compositions. The band of (Mg,Fe)O near the edge of the sample is interpreted to be a result of loss of Fe metal to the capsule (Fig. 5a). This band of (Mg,Fe)O may have acted as a physical barrier preventing further Fe loss from the sample, and consequently enabling the attainment of equilibrium.

The fO_2 of the experiment can be calculated based on the reaction $Fe+1/2O_2=FeO$ according to the calibration of O'Neill et al. (2003), with the composition of (Mg,Fe)O reflecting deviation from the IW buffer. The molar ratio of Mg/Fe in (Mg,Fe)O (~1) results in a calculated fO_2 of IW-0.6, i.e., QIF+0.2, at 3 GPa, 1050°C. Considering analytical and experimental uncertainties, this demonstrates that the assumption that BN imposed fO_2 conditions similar to that of the QIF buffer is valid for our experimental assembly.

The diffusion coefficient of Fe in Au

We are able to obtain the diffusion coefficient for Fe in Au by fitting the Fe concentration profile in the Au capsule of exp. LMD783 (Fig. 5c) to the following equation from Zhang (2010):

$$\ln C = \ln C_0 - \frac{x^2}{4Dt} \quad (8)$$

where x is the distance, t is time and D is the diffusion coefficient. This equation describes thin-source diffusion into a semi-infinite medium. By plotting $\ln C$ vs x^2, the coefficient of this linear trend can be used to derive the diffusion coefficient, with a resulting value of 1×10^{-13} m^2/s (Fig. 5d). Through fitting with the same equation, the Fe concentration profiles in both the inner and outer capsules of exp. LMD690 return slightly lower diffusion coefficients, 3×10^{-14} m^2/s and 5×10^{-14} m^2/s, respectively (Fig. 6). These values compare favorably with published diffusion coefficients at 1028°C: 1×10^{-12} m^2/s at 0.1 MPa in He (Duhl et al. 1963), 1×10^{-13} m^2/s at 5 GPa

298 in H_2, and 3×10^{-14} m^2/s at 5 GPa without H_2 (Yamazaki et al. 2004). Considering that the
299 diffusion coefficient at 5 GPa in H_2 is three times higher than that in the absence of H_2, the lower
300 values obtained for exp. LMD690 may be due to its more oxidized conditions compared to those
301 for exp. LMD783. The possibility that the profile for the inner capsule of exp. LMD690 may
302 have been affected by reverse diffusion of Fe from the sample and that Fe diffusion in the
303 capsule of exp. LMD783 may have reached its outer boundary represent other possible factors
304 contributing to the variation in obtained diffusion coefficients.
305

306 **Discussion**

307 **Determining fO_2 based on Fe content in Au capsules**

308 Calculating fO_2 based on the calibration from Ratajeski and Sisson (1999) has the advantage
309 of avoiding the uncertainties associated with calculating the FeO activity in hydrous rhyolitic
310 melt and the Fe activity in Au. However, the resultant fO_2 values are too high to be considered
311 reasonable. One possible cause is that the assumed fO_2 of FMQ-1 for the experiments of
312 Ratajeski and Sisson (1999) is overestimated. This possibility also agrees with the fact that
313 similar experiments from Patiño Douce and Beard (1994, 1995), performed without BN, have an
314 estimated fO_2 range of FMQ-2~FMQ. The calibration of Ratajeski and Sisson (1999) is similar
315 to the calibration for Fe partitioning between Pt metal and silicate melt obtained by Grove (1981).
316 However, the calibrations from Ratajeski and Sisson (1999) and Grove (1981) are not necessarily
317 equivalent considering the difference in γ_{FeO}^{melt} between rhyolitic melt and basaltic melt, and the
318 difference in γ_{Fe}^{alloy} between Fe-Au and Fe-Pt systems. Considering that Fe diffuses more readily
319 into Pt than Au at similar fO_2 conditions, the apparent equilibrium constant K' should have a
320 higher value for the Fe-Pt system than that for the Fe-Au system. Similar K' values obtained by

This is the peer-reviewed, final accepted version for American Mineralogist, published by the Mineralogical Society of America.
The published version is subject to change. Cite as Authors (Year) Title. American Mineralogist, in press.
DOI: https://doi.org/10.2138/am-2022-8577. http://www.minsocam.org/

Ratajeski and Sisson (1999) for the Fe-Au system can therefore be attributed to overestimated fO_2 (Eq. 4).

The fO_2 conditions for the equilibrium between FeO in melt and Fe in Au can be assessed in comparison to the calibration for the IW buffer by O'Neill (1988). Apart from the melt and alloy compositions, other parameters required include the equilibrium constant for the exchange reaction between the FeO melt component and the FeO solid phase (wustite), and activity coefficients ${\gamma_{FeO}}^{melt}$ and ${\gamma_{Fe}}^{metal}$, as demonstrated by the equation below:

$$\Delta IW = 2\log\left(\frac{X_{FeO}^{melt}}{X_{Fe}^{alloy}}\right) + 2\log\gamma_{FeO}^{melt} - 2\log\gamma_{Fe}^{alloy} - 2\log K(FeO^{melt} - FeO^{s}) \quad (9)$$

The estimated value is ~0.18 for $\log\gamma_{FeO}^{melt}$ based on the expression from O'Neill (2021), while the $\log K$ term for the FeO melt component and wustite exchange reaction is calculated to be -0.37 for the 3 GPa, 1050°C conditions of exp. LMD670, based on the thermodynamic database of Holland and Powell (2011). Although a positive deviation from ideal mixing has been observed for Fe-Au alloys at ambient pressures (Seigle 1956), the activity of Fe in the Au capsule is unknown for the very low Fe end of the Au-Fe solid solution. The low fO_2 for exp. LMD670 suggests that $\log\gamma_{Fe}^{alloy}$ has a positive value (~2).

When referring to redox sensors employing Fe alloys, Woodland and O'Neill (1997) state that "the method loses accuracy as the activity of Fe decreases, leading to unacceptably large errors when ${a_{Fe}}^{alloy}$ is less than about 0.1". This could also be the case for our experiments.

An explanation for the QIF-like intrinsic fO_2 conditions for our BN experiment

Both the comparability with the QIF-buffered experiment and direct fO_2 measurement using the Fe-(Mg,Fe)O sensor, suggest that BN in our experimental assembly imposed fO_2 conditions similar to that of the QIF buffer and thus far more reduced than the estimated FMQ-like

conditions assumed in previous studies. Such experimental studies used natural samples as their starting materials, which would have imposed higher fO_2 when compared to the reduced starting material used in our experimental series. However, as the difference in estimated fO_2 is so large, we suspect that this likely results from the difference in the intrinsic fH_2 of the experimental setup.

Truckenbrodt et al. (1997) investigated the redox conditions in piston-cylinder experiments employing fired BN or unfired pyrophyllite as packing materials surrounding the capsule in NaCl-graphite assemblies. They reported that C-O-H fluids from experiments using fired BN as a packing material maintained the initial fH_2 of the starting organic compounds ($C_4H_4O_4$, $C_9H_{10}O_2$, and $C_{14}H_{22}O$), while experiments with unfired pyrophyllite resulted in equivalent fH_2 for all three starting compositions, similar to cobalt-cobalt oxide (CoCoO)-buffered conditions, and representative of the intrinsic fH_2 of the NaCl-graphite assembly. This interesting result demonstrates that fired BN does not impose reduced fO_2 on the sample charge. This is likely due to the fact that heat treatment of BN increases its crystallinity and purity, and consequently reduces its ability to react with oxygen (Udayakumar et al. 2011). Moreover, their experimental results demonstrate that the dehydration of pyrophyllite is key for transmitting the intrinsic fH_2. Matjuschkin et al. (2015) state that "As pointed out by Luth (1989), the availability of H_2 to "transmit" any intrinsic fO_2 to the sample might depend on how well the larger parts of the assembly are dried or on the dehydration of talc if used as an assembly component." Under such a consideration, we may derive the following reaction describing the oxidation of BN involving H_2O:

$$2BN+3H_2O=B_2O_3+N_2+3H_2 \quad (10)$$

through the addition of the BN oxidation reaction (Eq. 1) and the H_2O dissociation reaction

367 $$H_2O=H_2+1/2O_2 \quad (11).$$

368 The fH_2 imposed by the BN sleeve is therefore a function of the H_2O activity, i.e., higher H_2O
369 activity, higher fH_2. Previously reported experiments in Li et al. (2021) were performed using a
370 cubic press. The experimental assembly used has a cylindrical configuration, similar to piston-
371 cylinder assemblies, but further encased in a pyrophyllite cube (Fig. 2). The more reduced
372 conditions observed in our BN experiment may be explained by a higher H_2O activity, which
373 may arise from dehydration of pyrophyllite in our experimental assembly.

374 The intrinsic H_2O activity of such assemblies remains unknown. At the commencement of
375 each run, gaskets form along the edges of the pyrophyllite cube during compression. If we can
376 consider the experimental assembly as a closed system after gasket formation, then H_2O activity
377 of the experimental assembly depends on the dehydration of pyrophyllite, and also the
378 consumption of H_2O due to BN oxidation. The BN oxidation reaction according to reaction (10)
379 produces both N_2 and H_2. The H_2 fugacity can be calculated by assuming similar conditions to
380 those imposed by the QIF buffer (O'Neill 1987) plus pure H_2O and subsequently the H_2 activity
381 can be estimated to be ~0.6. Based on the stoichiometry of reaction (10), and an assumption of
382 ideal mixing between gas species and similar fugacity coefficients, N_2 activity can be estimated
383 to be ~0.2. The H_2O activity is also ~0.2 if the gas phase is dominated by H_2, N_2 and H_2O. The
384 reduced N_2 activity implies that the fO_2 value would be ~1.4 log units lower than that of the QIF
385 buffer (Eq. 1), however, the similarly reduced H_2O activity means that fH_2 remains the same as
386 that of the QIF buffer (Eq. 10). There may be other gas species present, but not considered, for
387 example, CH_4, from the reaction of H_2O with graphite. Although much-simplified, such an
388 inverse modeling approach suggests that BN in our experimental assembly can maintain fH_2

similar to that of the QIF buffer plus H_2O, especially in the limiting case when a gas phase is present due to the dehydration of pyrophyllite.

The application of BN as an fO_2 control in solid media assemblies

The intrinsic fO_2 of our experimental assembly, using BN as a capsule sleeve and spacer, appears significantly more reduced than that reported by previous studies using common piston-cylinder assemblies containing BN. The primary difference lies in the usage of the pyrophyllite cube in our experimental setup. This represents a simple way to impose a reduced redox state relevant for investigating lunar conditions or reduced endmembers of the Martian environment, although the resultant chemical system will be H_2O-bearing. According to reaction (10), lowering H_2O activity will reduce or inhibit the BN oxidation reaction and its fO_2 buffering ability. Piston-cylinder experiments normally employ NaCl, talc or $BaCO_3$ tube as the pressure transmitting material encasing the graphite furnace, and MgO, Al_2O_3, pyrophyllite, BN or pyrex as assembly components within the graphite furnace. An available source of H_2O is required in order to impose the intrinsic fO_2 of the experimental assembly onto the sample charge. This could be either moisture absorbed by the pressure transmitting material, or H_2O from dehydration of talc and pyrophyllite.

The material immediately surrounding the capsule exerts the dominant control on the fO_2 of the sample. It is evident from previous studies that BN can impose more reduced conditions than MgO, which is useful when variation of fO_2 is a factor of research interest, although the exact value of fO_2 needs to be determined independently. The starting material can also have a buffering effect on fO_2 due to the exchange of H_2 between the sample and the assembly (Holloway et al. 1992). Whether it is the intrinsic fO_2 of the assembly or that of the sample which

This is the peer-reviewed, final accepted version for American Mineralogist, published by the Mineralogical Society of America.
The published version is subject to change. Cite as Authors (Year) Title. American Mineralogist, in press.
DOI: https://doi.org/10.2138/am-2022-8577. http://www.minsocam.org/

412 is desired, the redox potential between the sample and assembly can result in either gain or loss
413 of H_2O and Fe from the charge. Therefore, BN provides a suitable choice of pressure
414 transmitting material for reduced experimental redox conditions as it minimizes possible
415 modification of the starting composition.

416 A cautionary note on using BN as a pressure transmitting material: the experimental charge
417 may be contaminated with boron. As investigated and reported by Matjuschkin et al. (2015),
418 when BN powder was packed around a Pt capsule, 2000-3000 ppm boron was detected in glasses
419 produced from experiments run at 1200-1265°C for 24-26 hours. It appears that the magnitude of
420 boron contamination is similar to that of carbon infiltration (Matjuschkin et al. 2015). It is worth
421 keeping this issue in mind, especially for high temperature experiments.

422 An alternative approach to fO_2 control is to use the packing material surrounding the capsule
423 as a barrier between the capsule and assembly, in order to either maintain the redox state of the
424 sample or prolong the life of the oxygen buffer assemblage. Matjuschkin et al. (2015)
425 investigated the H_2 permeability of different pressure transmitting materials, and demonstrated
426 that pyrex functions better than MgO or Al_2O_3 at limiting the diffusion of H_2, therefore
427 maintaining the intended fH_2 within the capsule. The experimental results of Truckenbrodt et al.
428 (1997) suggest that fired BN also acts as an excellent H_2 barrier.

429

430 **Implications**

431 Controlling fO_2 in solid media assemblies is a challenging task. More often than not, the fO_2
432 of such experimental runs is not directly measured or controlled, but reflects the intrinsic fO_2 of
433 either the assembly or the sample, or somewhere in-between. The double-capsule configuration
434 employing a buffer assemblage is currently the most effective approach for achieving fO_2 control,

435 but requires a large capsule volume and is more difficult and time-consuming to prepare.
436 Therefore, imposing approximate fO_2 by selecting the appropriate capsule or pressure
437 transmitting material for the assembly is still the first choice for the majority of experimental
438 studies. Through our efforts to determine the fO_2 imposed by our chosen experimental assembly
439 using BN as a capsule sleeve, we are able to demonstrate the reducing ability of BN as an
440 assembly component, and furthermore shed light on the process by which BN imposes such
441 reduced fO_2. We hereby present what we have learnt during the course of this investigation, in
442 the hope that the effect of BN on fO_2 control is both recognized and further exploited in future
443 experimental studies.
444

445 **Acknowledgements**

446 The authors would like to thank Xiaoli Li from Peking University for his help with electron
447 microprobe analyses and Jesse Jones for helpful comments. Constructive reviews from Bruno
448 Scaillet and Vladimir Matjuschkin, and editorial handling by Antonio Acosta-Vigil are greatly
449 appreciated. This work is funded by the National Natural Science Foundation of China grant
450 41802052 to H.L..
451
452

453 **References cited**

454 Ardia, P., Hirschmann, M.M., Withers, A.C., and Stanley, B.D. (2013) Solubility of CH 4 in a
455 synthetic basaltic melt, with applications to atmosphere-magma ocean-core partitioning of
456 volatiles and to the evolution of the Martian atmosphere. Geochimica et Cosmochimica
457 Acta, 114, 52–71.

458 Armstrong, L.S., Hirschmann, M.M., Stanley, B.D., Falksen, E.G., and Jacobsen, S.D. (2015)
459 Speciation and solubility of reduced C–O–H–N volatiles in mafic melt: Implications for
460 volcanism, atmospheric evolution, and deep volatile cycles in the terrestrial planets.
461 Geochimica et Cosmochimica Acta, 171, 283–302.
462 Clemente, B., Scaillet, B., and Pichavant, M. (2004) The solubility of sulphur in hydrous
463 rhyolitic melts. Journal of Petrology, 45, 2171–2196.
464 Dalou, C., Hirschmann, M.M., Jacobsen, S.D., and Le Losq, C. (2019) Raman spectroscopy
465 study of C-O-H-N speciation in reduced basaltic glasses: Implications for reduced planetary
466 mantles. Geochimica et Cosmochimica Acta, 265, 32–47.
467 Dasgupta, R., Chi, H., Shimizu, N., Buono, A.S., and Walker, D. (2013) Carbon solution and
468 partitioning between metallic and silicate melts in a shallow magma ocean: Implications for
469 the origin and distribution of terrestrial carbon. Geochimica et Cosmochimica Acta, 102,
470 191–212.
471 Duhl, D., Hirano, K.-I., and Cohen, M. (1963) Diffusion of iron, cobalt and nickel in gold. Acta
472 Metallurgica, 11, 1–6.
473 Grewal, D.S., Dasgupta, R., and Farnell, A. (2020) The speciation of carbon, nitrogen, and water
474 in magma oceans and its effect on volatile partitioning between major reservoirs of the
475 Solar System rocky bodies. Geochimica et Cosmochimica Acta, 280, 281–301.
476 Grove, T.L. (1981) Use of FePt alloys to eliminate the iron loss problem in 1 atmosphere gas
477 mixing experiments: Theoretical and practical considerations. Contributions to Mineralogy
478 and Petrology, 78, 298–304.
479 Holland, T.J.B., and Powell, R. (2011) An improved and extended internally consistent
480 thermodynamic dataset for phases of petrological interest, involving a new equation of state

for solids. Journal of Metamorphic Geology, 29, 333–383.

Holloway, J.R., Pan, V., and Gudmundsson, G. (1992) High-pressure fluid-absent melting experiments in the presence of graphite: oxygen fugacity, ferric/ferrous ratio and dissolved CO2. European Journal of Mineralogy, 4, 105–114.

Kadik, A.A., Litvin, Y.A., Koltashev, V. V., Kryukova, E.B., and Plotnichenko, V.G. (2006) Solubility of hydrogen and carbon in reduced magmas of the early Earth's mantle. Geochemistry International, 44, 33–47.

Kadik, A.A., Koltashev, V. V., Kryukova, E.B., Plotnichenko, V.G., Tsekhonya, T.I., and Kononkova, N.N. (2015) Solubility of nitrogen, carbon, and hydrogen in FeO–Na2O–Al2O3–SiO2 melt and liquid iron alloy: Influence of oxygen fugacity. Geochemistry International, 53, 849–868.

Kadik, A.A., Kurovskaya, N.A., Lukanin, O.A., Ignat'ev, Y.A., Koltashev, V. V., Kryukova, E.B., Plotnichenko, V.G., and Kononkova, N.N. (2017) Formation of N–C–O–H molecules and complexes in the basalt–basaltic andesite melts at 1.5 Gpa and 1400°C in the presence of liquid iron alloys. Geochemistry International, 55, 151–162.

Li, H., and Zhang, L. (2022) A thermodynamic model for sulfur content at sulfide saturation (SCSS) in hydrous silicate melts: With implications for arc magma genesis and sulfur recycling. Geochimica et Cosmochimica Acta, 325, 187–204.

Li, H., Zhang, L., Bao, X., Wykes, J.L., and Liu, X. (2021) High sulfur solubility in subducted sediment melt under both reduced and oxidized conditions: With implications for S recycling in subduction zone settings. Geochimica et Cosmochimica Acta, 304, 305–326.

Li, Y., Dasgupta, R., and Tsuno, K. (2015) The effects of sulfur, silicon, water, and oxygen fugacity on carbon solubility and partitioning in Fe-rich alloy and silicate melt systems at 3

GPa and 1600 °C: Implications for core-mantle differentiation and degassing of magma oceans and reduced planet. Earth and Planetary Science Letters, 415, 54–66.

Li, Y., Dasgupta, R., Tsuno, K., Monteleone, B., and Shimizu, N. (2016) Carbon and sulfur budget of the silicate Earth explained by accretion of differentiated planetary embryos. Nature Geoscience, 9, 781–785.

Luth, R.W. (1989) Natural versus experimental control of oxidation state; effects on the composition and speciation of C-O-H fluids. American Mineralogist, 74, 50–57.

Matjuschkin, V., Brooker, R.A., Tattitch, B., Blundy, J.D., and Stamper, C.C. (2015) Control and monitoring of oxygen fugacity in piston cylinder experiments. Contributions to Mineralogy and Petrology, 169, 1–16.

Mysen, B.O. (1979) Nickel partitioning between olivine and silicate melt: Henry's law revisited. American Mineralogist, 64, 1107–1114.

Mysen, B.O., and Popp, R.K. (1980) Solubility of sulfur in CaMgSi 2 O 6 and NaAlSi 3 O 8 melts at high pressure and temperature with controlled f O2 and f S2. American Journal of Science, 280, 78–92.

Mysen, B.O., Fogel, M.L., Morrill, P.L., and Cody, G.D. (2009) Solution behavior of reduced C–O–H volatiles in silicate melts at high pressure and temperature. Geochimica et Cosmochimica Acta, 73, 1696–1710.

O'Neill, H.S.C. (1987) Quartz-fayalite-iron and quartz-fayalite-magnetite equilibria and the free energy of formation of fayalite (Fe2SiO4) and magnetite (Fe3O4). American Mineralogist, 72, 67–75.

——— (1988) Systems Fe-O and Cu-O : Thermodynamic data for the equilibria Fe-"FeO", Fe-Fe3O4, "FeO"-Fe3O4, Cu-Cu2O, and Cu2O-CuO from emf measurements. American

527 Mineralogist, 73, 470–486.
528 O'Neill, H.S.C. (2021) The Thermodynamic Controls on Sulfide Saturation in Silicate Melts
529 with Application to Ocean Floor Basalts. In R. Moretti and D.R. Neuville, Eds., Magma
530 redox geochemistry pp. 177–213. American geophysical union.
531 O'Neill, H.S.C., and Mavrogenes, J.A. (2002) The sulfide capacity and the sulfur content at
532 sulfide saturation of silicate melts at 1400°C and 1 bar. Journal of Petrology, 43, 1049–1087.
533 O'Neill, H.S.C., Pownceby, M.I., and McCammon, C.A. (2003) The magnesiow□stite: iron
534 equilibrium and its implications for the activity-composition relations of (Mg,Fe)2SiO4
535 olivine solid solutions. Contributions to Mineralogy and Petrology, 146, 308–325.
536 Ohmoto, H., and Kerrick, D.M. (1977) Devolatilization equilibria in graphitic systems. American
537 Journal of Science, 277, 1013–1044.
538 Patiño Douce, A.E., and Beard, J.S. (1994) H2O loss from hydrous melts during fluid-absent
539 piston cylinder experiments. American Mineralogist, 79, 585–588.
540 Patiño Douce, A.E., and Beard, J.S. (1995) Dehydration-melting of biotite gneiss and quartz
541 amphibolite from 3 to 15 kbar. Journal of Petrology, 36, 707–738.
542 Pelleter, A.A., Prouteau, G., and Scaillet, B. (2021) The Role of Sulphur on the Melting of Ca-
543 Poor Sediment and on Trace Element Transfer in Subduction Zones: An Experimental
544 Investigation. Journal of Petrology, 62, 1–42.
545 Plank, T., and Langmuir, C.H. (1998) The chemical composition of subducting sediment and its
546 consequences for the crust and mantle. Chemical Geology, 145, 325–394.
547 Ratajeski, K., and Sisson, T.W. (1999) Loss of iron to gold capsules in rock-melting experiments.
548 American Mineralogist, 84, 1521–1527.
549 Seigle, L.L. (1956) Thermodynamic Properties of Solid Fe-Au Alloys. JOM, 8, 91–97.

Sisson, T.W., Ratajeski, K., Hankins, W.B., and Glazner, A.F. (2005) Voluminous granitic magmas from common basaltic sources. Contributions to Mineralogy and Petrology, 148, 635–661.

Truckenbrodt, J., Ziegenbein, D., and Johannes, W. (1997) Redox conditions in piston cylinder apparatus: The different behavior of boron nitride and unfired pyrophillite assemblies. American Mineralogist, 82, 337–344.

Udayakumar, A., Sri Ganesh, A., Raja, S., and Balasubramanian, M. (2011) Effect of intermediate heat treatment on mechanical properties of SiCf/SiC composites with BN interphase prepared by ICVI. Journal of the European Ceramic Society, 31, 1145–1153.

Wendlandt, R.F., Huebner, J.S., and Harrison, W.J. (1982) The redox potential of boron nitride and implications for its use as a crucible material in experimental petrology. American Mineralogist, 67, 170–174.

Woodland, A.B., and O'Neill, H.S.C. (1997) Thermodynamic data for Fe-bearing phases obtained using noble metal alloys as redox sensors. Geochimica et Cosmochimica Acta, 61, 4359–4366.

Yamazaki, Y., Iijima, Y., and Okada, M. (2004) Diffusion of Fe in Au under elevated H2 pressure. Philosophical Magazine Letters, 84, 165–174.

Zhang, Y. (2010) Diffusion in minerals and melts: Theoretical background. Reviews in Mineralogy and Geochemistry, 72, 5–59.

Figure captions:

Fig. 1 A comparison of the Raman spectra of quenched melt from the BN experiment LMD670, the MW-buffered exp. LMD690 and the QIF-buffered exp. LMD776.

573 Fig. 2 A schematic diagram of the experimental cubic press assembly used for our experiments.

574 Fig. 3 The Fe content profiles in both inner and outer Au capsules for the BN experiment
575 LMD670 (a), the MW-buffered exp. LMD690 (b, c), and the QIF-buffered exp. LMD776 (d,
576 e). Note that scales for the y axis vary between graphs for different experiments. The
577 variation in profile length reflects the variability of capsule width, both regionally within
578 each capsule and between capsules from individual experiments, caused by the compression
579 encountered during experimental runs. The two profiles for exp. LMD670 represent data
580 obtained from firstly a position closer to the center of the capsule (red line) and secondly a
581 distal position (blue line). The temperature gradient may explain the smoother profile for
582 the hotter position (red line).

583 Fig. 4 lnS (ppm) versus $\ln X_{FeO}$ in melt for 3 GPa, 1050°C experiments reported previously in Li
584 et al. (2021) and exp. LMD776 from this study. Note that the fitting of the trendline is based
585 on previous experiments.

586 Fig. 5 Stereoscopic photos of exp. LMD783 showing (a) the diffusion of Fe into the Au capsule
587 and (b) the intergrowth of Fe metal and (Mg,Fe)O. The Fe diffusion profile is plotted in (c).
588 The fitting of the Fe diffusion profile to equation (8) is shown in (d).

589 Fig. 6 The fitting of Fe diffusion profiles in both the inner (a) and outer (b) capsules from exp.
590 LMD690 to equation (8). Note that *x* represents the distance measured from the buffer for
591 both profiles. The profile from the inner capsule of exp. LMD690 is shown in blue in Fig.
592 3b with the first 40 μm section excluded for the purpose of fitting.

593

594 Supplementary figures:

595 Fig. S1 The positions for Fe in Au profiles shown as arrows for exp. LMD670 (a), LMD690 (b)

596 and LMD776 (c). Arrow colors correspond to the color of the profiles in Fig. 3. The black
597 rectangle in (c) outlines the magnified area shown in (d). Mineral abbreviations: Coe,
598 Coesite; Fs, ferrosilite; Ol, olivine.

599 Supplementary data tables:

600 Table S1 Raw data for Fe diffusion profiles.

601 Table S2 Fe content in Au capsules in contact with the sample charge.

602 Table S3 Phase compositions in exp. LMD776.

603 Table S4 Phase compositions in exp. LMD783.

604

605

606

607

608 Table 1 Summary of experimental conditions and run products.
609

Exp. No.	Starting comp.	*P*(GPa)	*T*(°C)	Time (hours)	Buffer	Estimated fO_2	Phase assemblage
[a]LMD670	EPSM-S1	3	1050	96	BN sleeve	FMQ-7.5	melt [b](95) Po [c]*Grt Coe Ap*
LMD690	EPSM-S1	3	1050	46	MW	FMQ-3.8	melt (95) Po Grt Coe Ap Gr
LMD776	EPSM-S1	3	1050	48	QIF	FMQ-7.5	melt (85) Po Grt Coe Ap
[a]LMD783	Fe+$Mg(OH)_2$	3	1050	24	BN sleeve	FMQ-5.2	Fe, (Mg,Fe)O

610
611 Mineral abbreviations: Ap, apatite; Coe, Coesite; Gr, graphite; Grt, garnet; Po, pyrrhotite.
612 Buffer abbreviations: QIF: quartz-iron-fayalite; MW, magnetite-wustite; FMQ: fayalite-magnetite-quartz.
613 [a]No buffers were employed in these experiments.
614 [b]Numbers in brackets following "melt" are melt percentages in the charge, estimated by sight.
615 [c]Mineral phases in italics appear at the colder end of the capsule only.
616

Figure 1

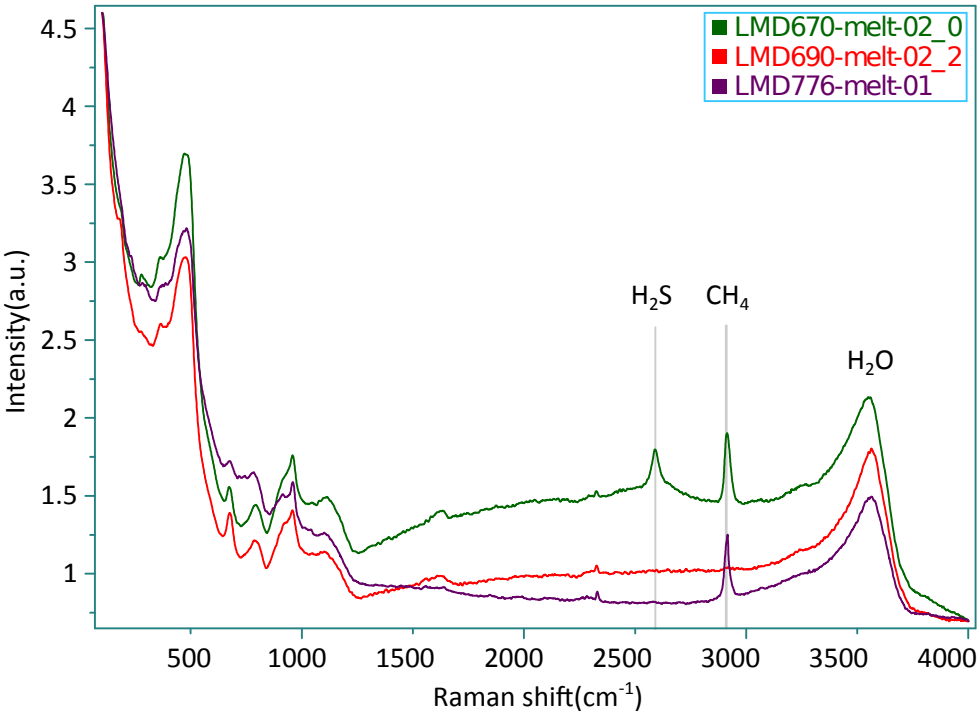

Fig.2

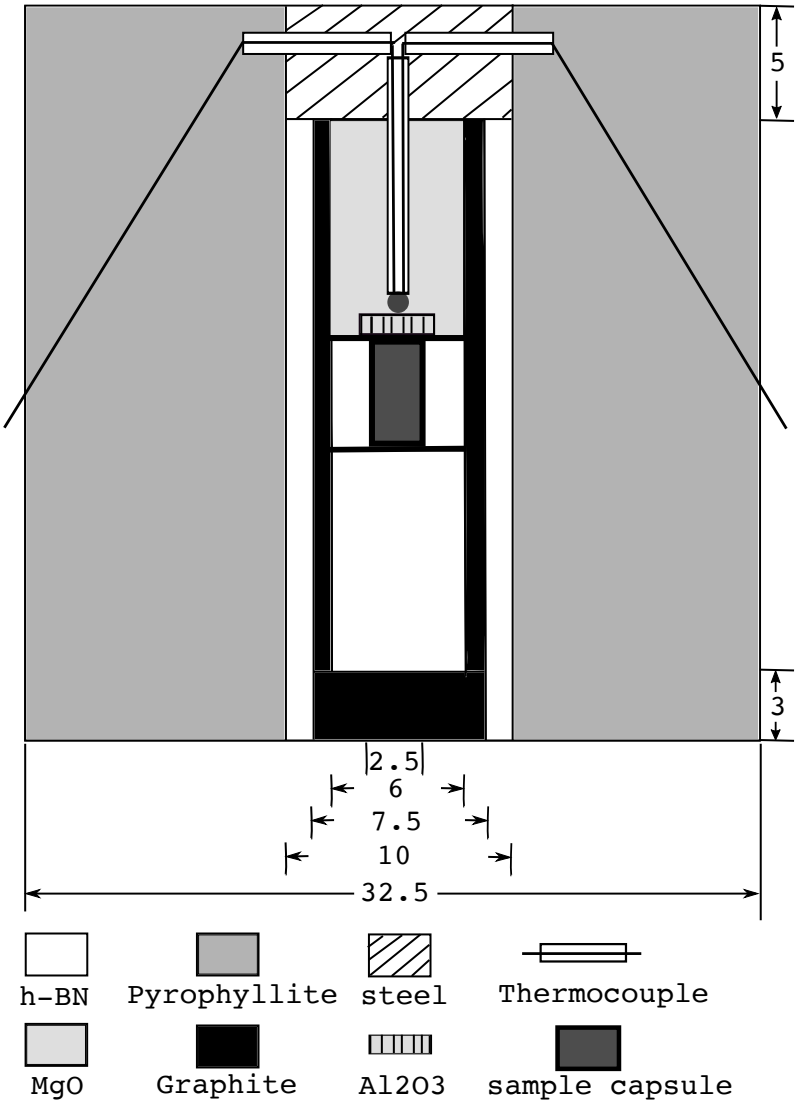

This is the peer-reviewed, final accepted version for American Mineralogist, published by the Mineralogical Society of America.
The published version is subject to change. Cite as Authors (Year) Title. American Mineralogist, in press.
DOI: https://doi.org/10.2138/am-2022-8577. http://www.minsocam.org/

Fig. 3

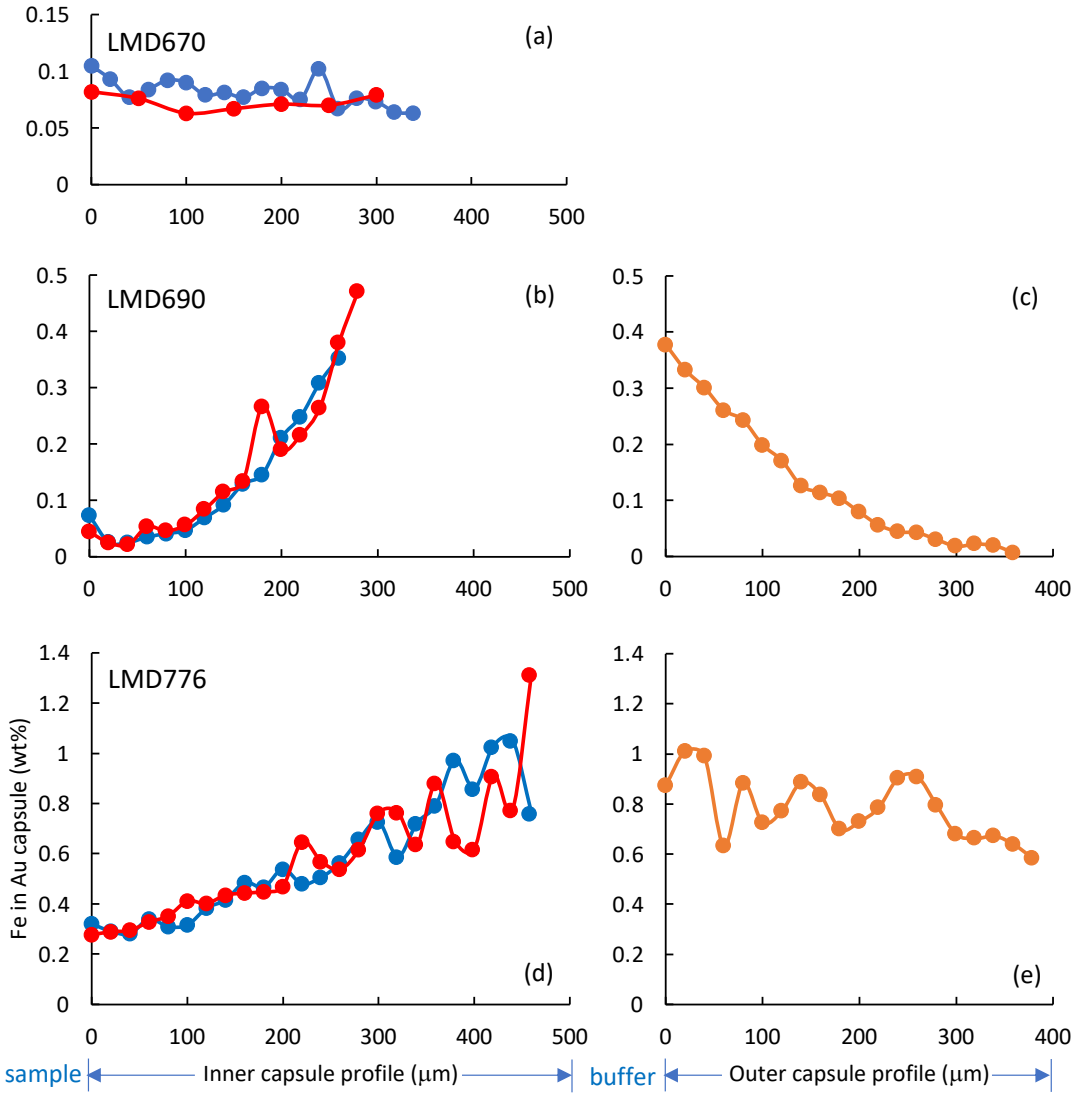

This is the peer-reviewed, final accepted version for American Mineralogist, published by the Mineralogical Society of America.
The published version is subject to change. Cite as Authors (Year) Title. American Mineralogist, in press.
DOI: https://doi.org/10.2138/am-2022-8577. http://www.minsocam.org/

Fig. 4

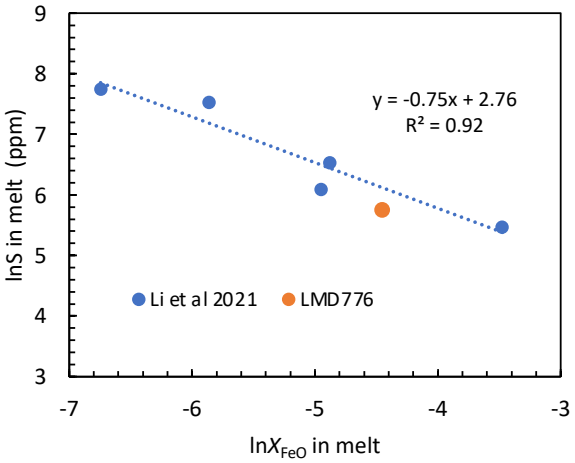

This is the peer-reviewed, final accepted version for American Mineralogist, published by the Mineralogical Society of America.
The published version is subject to change. Cite as Authors (Year) Title. American Mineralogist, in press.
DOI: https://doi.org/10.2138/am-2022-8577. http://www.minsocam.org/

Fig. 5

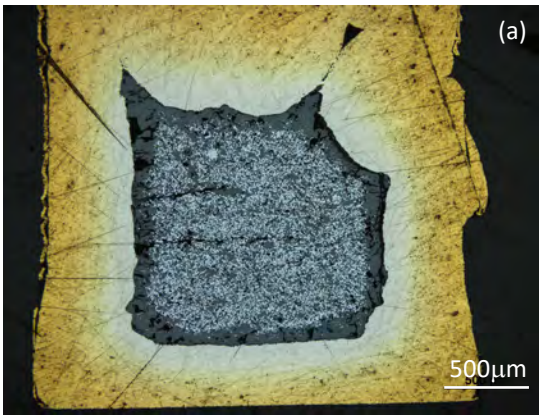

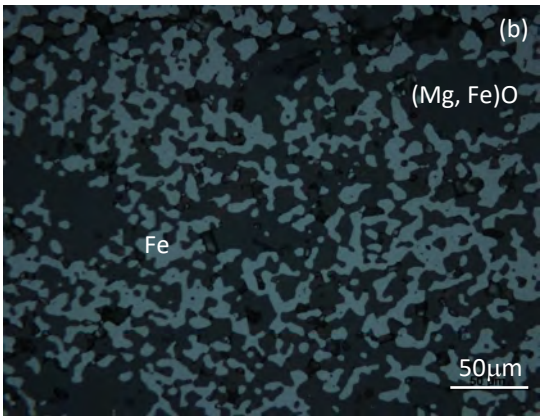

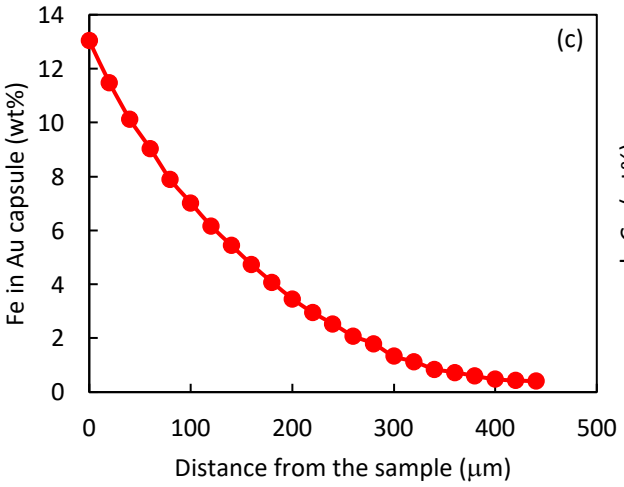

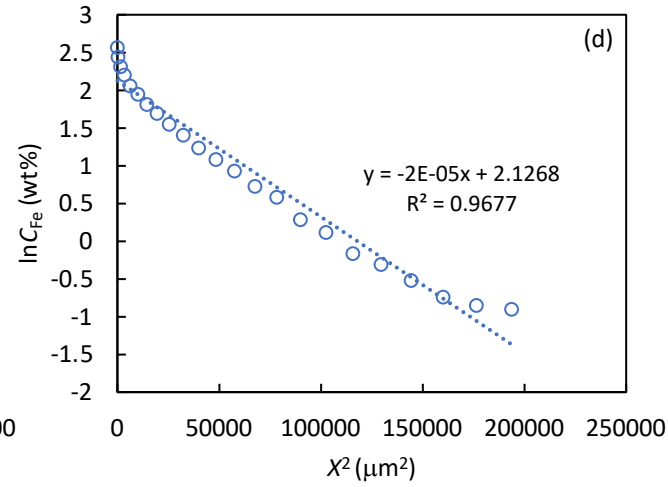

This is the peer-reviewed, final accepted version for American Mineralogist, published by the Mineralogical Society of America.
The published version is subject to change. Cite as Authors (Year) Title. American Mineralogist, in press.
DOI: https://doi.org/10.2138/am-2022-8577. http://www.minsocam.org/

Fig. 6